ACS APPLIED MATERIALS & INTERFACES

Research Article

www.acsami.org

Synthesis of Nitrogen-Doped MnO/Graphene Nanosheets Hybrid Material for Lithium Ion Batteries

Kejun Zhang,[†] Pengxian Han,[†] Lin Gu,[‡] Lixue Zhang,[†] Zhihong Liu,[†] Qingshan Kong,[†] Chuanjian Zhang,[†] Shanmu Dong,[†] Zhongyi Zhang,[†] Jianhua Yao,[†] Hongxia Xu,[†] Guanglei Cui,*[,†] and Liquan Chen[†,‡]

[†]Qingdao Institute of Bioenergy and Bioprocess Technology, Chinese Academy of Sciences, Qingdao 266101, P. R. China

[‡]Institute of Physics, Chinese Academy of Sciences, Beijing 100080, P. R. China

Supporting Information

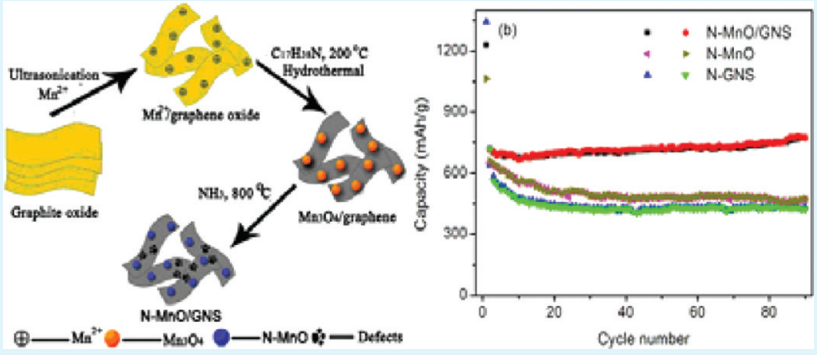

ABSTRACT: Nitrogen-doped MnO/graphene nanosheets (N-MnO/GNS) hybrid material was synthesized by a simple hydrothermal method followed by ammonia annealing. The samples were systematically investigated by X-ray diffraction analysis, Raman spectroscopy, X-ray photoelectron spectroscopy, transmission electron microscopy, and atomic force microscopy. N-doped MnO (N-MnO) nanoparticles were homogenously anchored on the thin layers of N-doped GNS (N-GNS) to form an efficient electronic/ionic mixed conducting network. This nanostructured hybrid exhibited a reversible electrochemical lithium storage capacity as high as 772 mAh g^{-1} at 100 mA g^{-1} after 90 cycles, and an excellent rate capability of 202 mA h g^{-1} at a high current density of 5 A g^{-1}. It is expected that N-MnO/GNS hybrid could be a promising candidate material as a high capacity anode for lithium ion batteries.

KEYWORDS: *nitrogen-doped MnO, nitrogen-doped graphene nanosheets, surface defects, anode material, lithium ion batteries*

INTRODUCTION

Nanomaterials of transition metal oxides, such as NiO,[1−3] Co_3O_4,[1,4,5] MoO_2,[6,7] and FeO_x,[8,9] have been intensively studied as anode materials for lithium ion batteries (LIBs) aimed at achieving higher specific capacities than commercial graphite. For instance, NiO nanocrystals have been explored for LIB anodes with specific capacities almost 2 times higher than that of graphite.[3] Compared to NiO, MnO is an attractive anode material for LIBs because of its low cost, environmental benignity, and the high abundance of Mn. However, the exploration of MnO as an anode material is hampered because of its poor electronic conductivity, volume expansion, and severe aggregation during the cycling processes, which result in a large irreversible capacity loss and poor rate performance.[10] Although a variety of appealing strategies including the carbon-coating and thin film structure have been utilized to solve these problems,[11−14] it still remains a great challenge for MnO electrode material to obtain large reversible capacity combined with long cycling life and good rate capability.

Graphene is an excellent substrate to host active nanomaterials for energy applications because of its superior conductivity, structure flexibility, large surface area, and chemical stability.[15−19] Some attempts have been made to use graphene as electronic conducting framework to improve the lithium storage capacity. In this regard, SnO_2/graphene,[20] Co_3O_4/graphene,[21] Fe_3O_4/graphene,[22] and Mn_3O_4/graphene[23] hybrids or composites are proved to be able to improve rate capacity and enhance the cycle life. Recently, nitrogen-doped graphene nanosheets (N-GNS) have been explored by ammonia annealing of graphite oxide (GO) or by chemical vapor deposition method for lithium storage,[24,25] which showed better electrochemical performance than bare graphene. The well-bonded nitrogen atoms could offer more active sites, which enhanced the interaction between the formed carbon structure and lithium, and thus improved the kinetics of lithium

Received: August 31, 2011
Accepted: January 2, 2012
Published: January 2, 2012

diffusion and transfer.[26,27] To the best of our knowledge, an anode material combining N-doped MnO (N-MnO) and N-GNS based materials for LIBs has been scarcely reported. It is expected that the N-MnO/GNS hybrid can effectively utilize the combinative merits of nanosized N-MnO and electrically conductive N-GNS to obtain superior performance for LIBs.

Herein, we report a simple method to synthesize N-MnO/GNS hybrid material for high performance LIB anode. This nanostructured hybrid displays superior electrochemical performance with large reversible capacity, high Coulombic efficiency, excellent cyclic performance and good rate capacity, which exhibits a great potential as anode material in LIBs.

EXPERIMENTAL SECTION

Synthesis of N-MnO/GNS Hybrid. GO was prepared using graphite powder (Aldrich, powder, < 20 μm, synthetic) according to Hummers method.[28] N-MnO/GNS hybrid was synthesized by a simple hydrothermal method combined with a heat treatment at 800 °C under ammonia atmosphere (as shown in Figure 1). In a typical procedure, GO was mixed with $Mn(NO_3)_2$ solution (50 wt %), and followed by stirring and sonication at room temperature for 2 h. Then 18 mL oleylamine was added to the above solution under stirring. The mixture was sealed in an autoclave and kept at 200 °C for 24 h to obtain Mn_3O_4 particles embedded in the graphene (Mn_3O_4/graphene), as shown in Figure S1 in the Supporting Information. The hybrid was characterized by X-ray diffraction (XRD) measurement (see Figure S2 in the Supporting Information), which showed that all the diffraction peaks were consistent with the standard values for Mn_3O_4 (JCPDS NO. 24–0734). The resultant Mn_3O_4/graphene hybrid was dried at 70 °C for 24 h, and then calcinated at 800 °C for 5 h under NH_3 atmosphere to get the N-MnO/GNS hybrid material. According to the elemental analysis, the weight percentage of N-GNS content is 8.9% in the N-MnO/GNS hybrid.

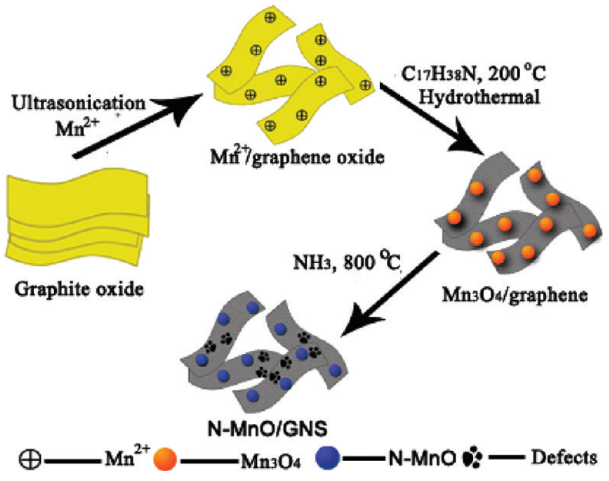

Figure 1. Schematic Illustration for the Preparation of N-MnO/GNS Hybrid Material.

Synthesis of N-MnO and H-MnO. N-MnO was also obtained by the same procedure without adding GO. The pure MnO electrode (H-MnO) was obtained from Mn_3O_4 calcinated at 800 °C under an H_2/Ar atmosphere (see Figure S3 in the Supporting Information).

Materials Characterization. XRD analysis of N-MnO/GNS hybrid was performed on a Bruker-AXS Microdiffractometer (D8 ADVANCE) with Cu Kα radiation (λ =1.5406 Å) from 20 to 80°. Raman spectra were recorded on a JY HR800 Raman spectrophotometer (Horiba Jobin Yvon, France) with 532 nm diode laser excitation. X-ray photoelectron spectroscopy (XPS) was acquired using an ESCALab220i-XL spectrometer (VG Scientific) with Al Kα radiation in twin anode at 14 kV × 16 mA. Elemental analysis was performed on a Flash EA 1112 CHNS/O elemental analyzer from Thermo Scientific. The UV–Vis reflection spectra of the MnO particles were measured by using a spectrophotometer (JASCO V-570). The morphology of the samples was analyzed using a Hitachi S-4800 scanning electron microscopy (SEM), a JEOL 2011F transmission electron microscope (TEM) and an Aglient 5400 atomic force microscope (AFM), respectively.

Electrochemical Measurements. Electrochemical experiments were carried out using standard R2032 type coin cells. The working electrodes were prepared by mixing 85 wt % active material with 5 wt % conductive carbon black and 10 wt % polyvinylidene fluoride dissolved in N-methyl-2-pyrrolidone. The slurry was then coated onto a copper foil and dried in a vacuum oven at 120 °C for 12 h. Pure lithium foil was used as the counter electrode. The electrolyte was 1 M $LiPF_6$ in ethylene carbonate/dimethyl carbonate (1:1 by volume), and Celgard 2400 membrane was uesd as the separator. The cells were assembled in an argon-filled glovebox. Galvanostatical discharge–charge experiments were performed at different current densities in the voltage range between 3.00 and 0.01 V. Cyclic voltammetry (CV) curves were carried out on ZAHNER ZENNIUM electrochemical workstation at a scanning rate of 0.5 mV s^{-1}. Alternating current (AC) impedance was recorded by applying a sine wave with an amplitude of 5.0 mV over the frequency range from 100 kHz to 100 mHz. The code Zview was used to fit the impedance spectra to the proposed equivalent circuit.

RESULTS AND DISCUSSION

X-ray diffraction patterns of the N-MnO/GNS hybrid material are shown in Figure 2a, in which all strong peaks in the XRD pattern can be indexed as a cubic phase of MnO (JCPDS No. 78–0424). The lattice parameters calculated from the XRD pattern are 4.444 Å ($a = b = c$) for N-MnO, which are larger than that of MnO (4.442 Å, JCPDS 78–0424) as a result of N-doping. Raman spectrum of the hybrid material is shown in Figure 2b. The Raman scattering peak observed at 637 cm^{-1} should be corresponded to the Mn–O vibration mode.[29] The broad peaks displayed at 1356 and 1600 cm^{-1} are assigned to the D and G bands of N-GNS, respectively. The D band is related to the mode of the k-point phonons of A_{1g} symmetry while the G band corresponds to the zone center E_{2g} phonon of C_{sp2} atoms.[30] The high intensity of the D band clearly indicates the presence of defects in the hybrid, which should be caused by N-doping in the GNS.[31] A broad and weak 2D band is observed at 2697 cm^{-1}, which is an overtone of the disorder induced D band and sensitive to the number of layers. The Raman spectrum reveals that few-layered N-GNS with some defects is successfully obtained, which should be favorable to the improvement of the electrochemical properties.

Further information on the composition of the as-prepared hybrid was obtained from XPS measurement (Figure 2c). The XPS analysis shows the presence of the principal C 1s (284.7 eV), O 1s (531.8 eV), Mn 2p (642.2 and 653.4 eV) and N 1s (397.5, 399.1, and 402.7 eV) core levels.[32] The Mn 2p XPS spectrum exhibits two characteristic peaks at 642.2 and 653.4 eV, corresponding to the Mn $2p_{3/2}$ and Mn $2p_{1/2}$ spin–orbit peaks of MnO (see Figure S4 in the Supporting Information).[33] The C 1s core level can be resolved into four components centered at ~284.7, 285.5, 286.5, and 289.0 eV, representing sp^2–sp^2C, N-sp^2C, N-sp^3C and C–O type bonds,[34] respectively (inset in Figure 2c). Similarly, the N 1s peak can also be resolved into three components centered at 397.5, 399.1, and 402.7 eV, representing pyridinic, pyrrolic, and graphitic types of atoms doped in the graphene structure (Figure 2d).[32,34] The XPS spectrum of N-MnO prepared under the same conditions without adding GO is shown in Figure S4

dx.doi.org/10.1021/am201173z | ACS Appl. Mater. Interfaces 2012, 4, 658–664

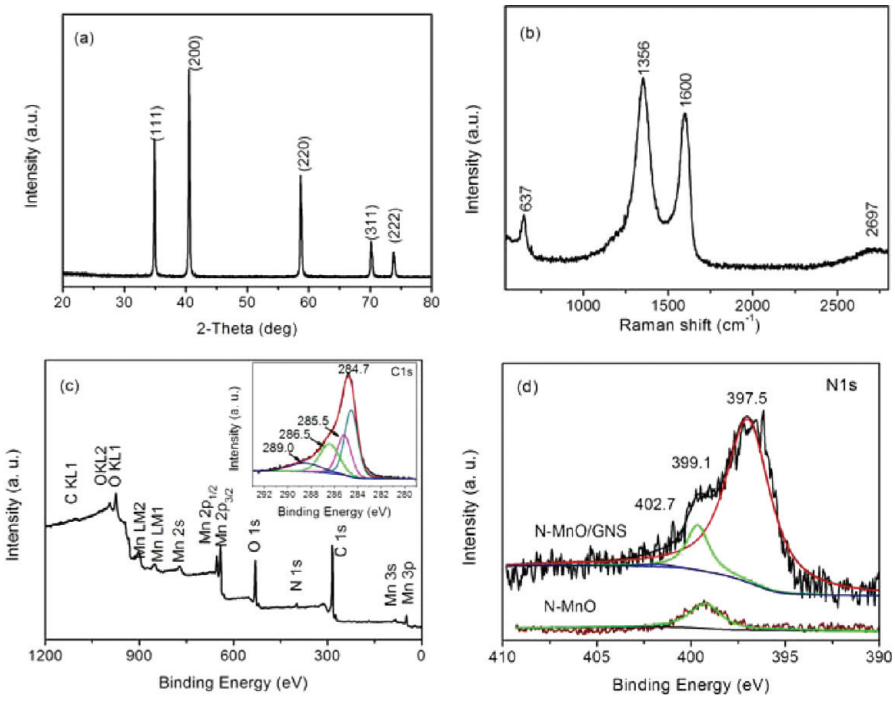

Figure 2. (a) XRD pattern, (b) Raman spectrum, and (c) XPS spectrum of the N-MnO/GNS hybrid, (d) N 1s XPS of the N-MnO/GNS hybrid and N-MnO. The inset in c is the C 1s XPS of the N-MnO/GNS hybrid.

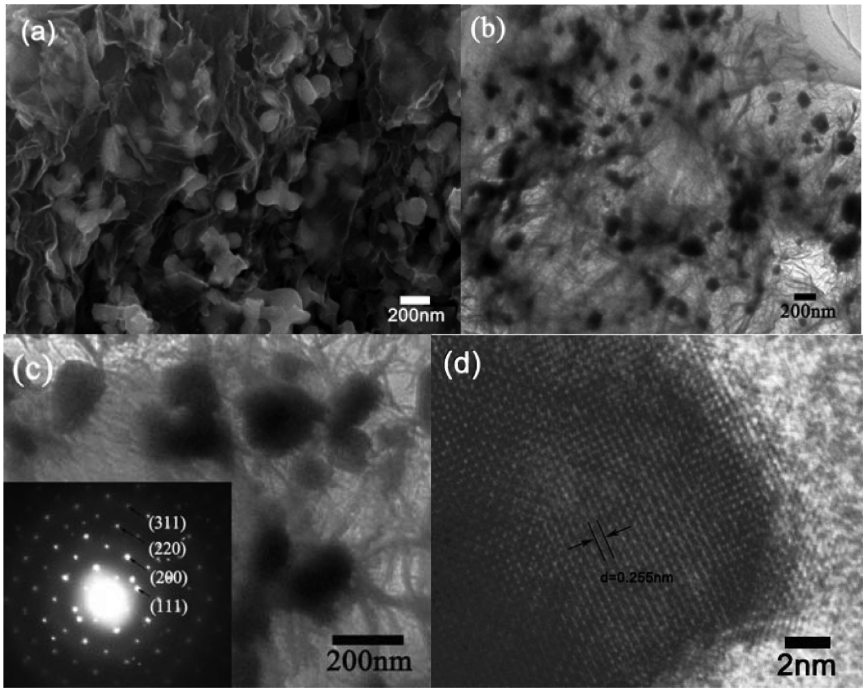

Figure 3. (a) SEM image of N-MnO/GNS hybrid material, (b) low-magnification TEM, (c) high-magnification TEM, and (d) high-resolution TEM image of N-MnO/GNS hybrid material. The inset in c is the SAED pattern of N-MnO in the N-MnO/GNS hybrid material.

in the Supporting Information. Besides the Mn 2p and oxygen O 1s signals from N-MnO, the N 1s peak observed around 399.2 eV is assigned to the O−Mn−N linkages in MnO lattice.[35] Therefore, it is deduced that nitrogen was doped into MnO lattices by substituting the oxygen atoms. This result is further confirmed by UV−Vis spectrometry,[36] besides a characteristic absorption band of MnO appears at 610 nm, the absorption band of N-MnO shows a little shift compared with H-MnO as a result of N-doping in the MnO, as shown in Figure S5 in the Supporting Information. In addition, the N dopant amounts calculated using the elemental analysis are 1.13 and 0.46 wt % for N-MnO/GNS and N-MnO, respectively (see Table S1 in the Supporting Information).

The microstructure of the N-MnO/GNS hybrid material was characterized by SEM and TEM. It can be seen from Figure 3a that the hybrid material possesses a layered structure consisting of N-GNS and N-MnO nanoparticles. The TEM images (Figure 3b, c) reveal that the N-MnO nanoparticles ranging

dx.doi.org/10.1021/am201173z | ACS Appl. Mater. Interfaces 2012, 4, 658−664

from 120 to 200 nm in diameter are homogenously attached on the thin N-GNS layers. The selected area electron diffraction (SAED) pattern (inset in Figure 3c) and high resolution TEM image (Figure 3d) clearly demonstrate the well-textured and single-crystalline nature of N-MnO in the hybrid, which is consistent with the XRD measurements. It should be noted that, for the bare N-MnO sample prepared without GO addition, only larger particles are obtained (see Figure S6 in the Supporting Information). In our experiment, N-MnO nanoparticles adhering on N-GNS are obtained. It is speculated that the absorption of Mn ions onto the GO plays a critical role, because the uniform distribution of ions restricts the aggregation of small crystal to grow larger in the formation process of hybrid (Mn_3O_4/graphene). So, when the Mn_3O_4/graphene hybrid is annealed under ammonia atmosphere, graphene restricts the aggregation of small N-MnO crystal during the crystal formation process. AFM image of the N-MnO/GNS hybrid reveals the surface traces of N-GNS and N-MnO. As shown in Figure 4a, N-MnO nanoparticles are identified as bright dots, some of which are deposited on the surface of N-GNS. The height profile acrossed the sample show that the thickness of the N-GNS is about 2.8 nm (Figure 4b), further confirming the formation of several layers of graphene nanosheets.

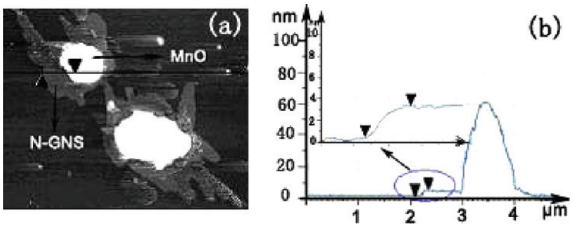

Figure 4. (a) Tapping-mode AFM image and (b) the corresponding height profile of N-MnO/GNS hybrid material derived from a. The thickness of N-GNS is around 2.8 nm.

Lithium storage properties of the N-MnO/GNS and N-MnO electrodes are investigated by performing galvanostatic discharge–charge and CV experiments. Figure 5a, b shows the discharge–charge curves of the N-MnO/GNS and N-MnO electrodes at a current density of 50 mA g^{-1}. During the first discharge process, the N-MnO/GNS hybrid and N-MnO present a long voltage plateau at about 0.10 V and then decrease slowly to 0.01 V, associated with the complete reduction of Mn^{2+} to Mn^0. For the initial charge curve, a slope in the voltage range between 1.0 and 1.5 V is related to the oxidation of Mn^0 to Mn^{2+}, which is an indicator of typical characteristic of voltage trends of the MnO electrode.[12,14,37] The initial discharge capacities of the N-MnO and N-MnO/GNS are 1188 and 1193 mAh g^{-1}, respectively. The N-MnO/GNS hybrid shows higher initial Coulombic efficiency (69.5%) than N-MnO (63.1%). The initial capacity loss may result from the incomplete conversion reaction and the irreversible lithium loss due to the formation of a solid electrolyte interphase (SEI) layer.[37] From the second cycle, the N-MnO/GNS hybrid electrode presents a much better electrochemical lithium storage performance than N-MnO electrode. Figure 5c, d present CV curves of N-MnO/GNS hybrid and N-MnO electrodes, respectively. In the first cycle, cathodic peak at 0.42 and 0.56 V are observed for the N-MnO/GNS hybrid material and N-MnO respectively, corresponding to the electrochemical reduction reaction of MnO with Li. The observed main anodic

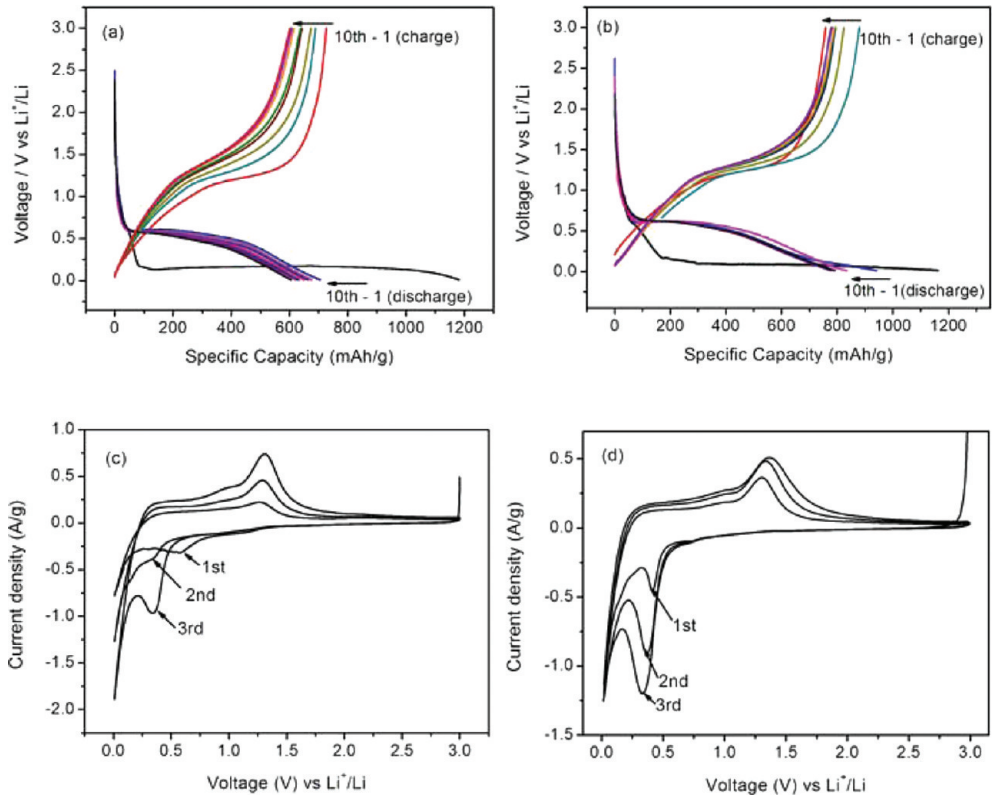

Figure 5. First ten discharge–charge curves of (a) N-MnO and (b) N-MnO/GNS electrodes at a current density of 50 mA g^{-1}. CV curves of (c) N-MnO and (d) N-MnO/GNS electrodes at a scan rate of 0.5 mV s^{-1} during the first three cycles.

dx.doi.org/10.1021/am201173z | ACS Appl. Mater. Interfaces 2012, 4, 658–664

peaks observed at 1.28 V for the N-MnO/GNS hybrid and 1.32 V for N-MnO are ascribed to the oxidation reaction. From the second cycle, the main reduction current peaks shift to 0.37 V for the N-MnO/GNS hybrid and to 0.33 V for N-MnO, indicating an irreversible phase transformation due to the formation of Li_2O and Mn.[37]

To further investigate the electrochemical performance of N-MnO/GNS hybrid and N-MnO, we show the rate capability and cycling performance of the samples in Figure 6. The

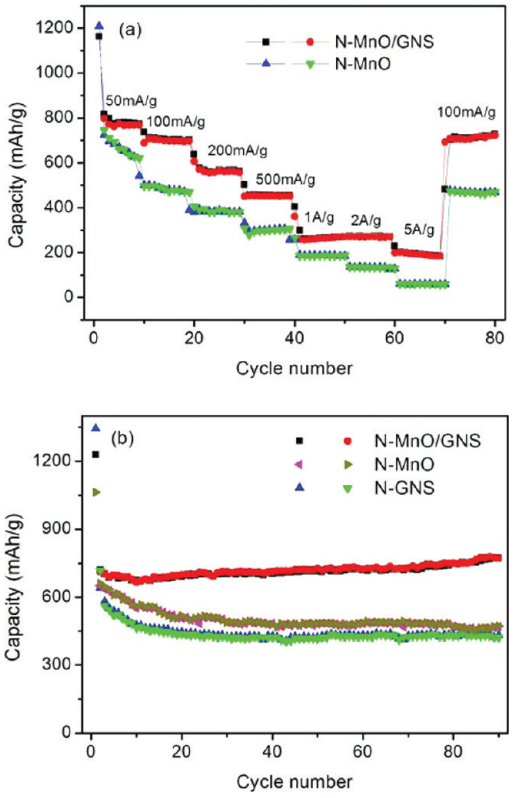

Figure 6. (a) Rate capability of N-MnO and N-MnO/GNS at various current densities, (b) comparison of cycling performance of N-MnO, N-GNS, and N-MnO/GNS hybrid at a current density of 100 mA g^{-1}.

reversible capacity of N-MnO/GNS is around 789 mA h g^{-1} after a few cycles at 50 mA g^{-1}, whereas the corresponding value for N-MnO is 622 mA h g^{-1}. When the current density reaches 5 A g^{-1}, the specific capacity of N-MnO/GNS hybrid still remains 202 mA h g^{-1} (Figure 6a), which is approximately 3 times higher than that value for the N-MnO electrode. Figure 6b depicts the discharge−charge cycling performance of the N-MnO/GNS hybrid, N-GNS, and N-MnO at a current density of 100 mA g^{-1} for 90 cycles. The reversible capacities of N-MnO decrease from 678 to 464 mA h g^{-1} and N-GNS decrease from 588 to 420 mA h g^{-1}. In contrast, the reversible capacities of N-MnO/GNS hybrid slightly increase with cycling and reach 772 mA h g^{-1} after 90 cycles, which is much higher than that of bare N-GNS and N-MnO samples. It was reported by J. M. Tarascon that metal oxide suffered from an increasing capacity with cycling, which should be due to formation of a polymeric gel-like film resulting from kinetically activated electrolyte degradation during conversion process.[38] In addition, there could be a synergetic effect between conducting N-GNS and N-MnO particles in the hybrid.[39] To elucidate the role of doped nitrogen in the hybrid, we also investigated the performance of MnO/graphene (no N-doping) material. As shown in Figure S7 in the Supporting Information, N-MnO/GNS hybrid possesses better rate capability than MnO/graphene, which confirms the advantage of doped nitrogen in the hybrid.

The electrochemical impedance of the N-MnO and N-MnO/GNS electrodes was performed (Figure 7). Figure 7a clearly shows that the diameter of semicircle for N-MnO/GNS electrode in the high medium frequency region is much smaller than that of bare N-MnO electrode, suggesting that N-MnO/GNS electrode possess a lower charge transfer resistance. The kinetic differences of N-MnO/GNS electrode before cycling and after 10 cycles are further investigated by modeling AC impedance spectra based on the modified equivalent circuit (Figure 7b).[40,41] In the equivalent circuit, R_e is the total resistance of electrolyte, electrode and separator. CPE_1 and R_f are the capacitance and resistance of the surface film formed on the electrode, respectively. CPE_2 and R_{ct} are the double layer capacitance and charge transfer resistance, respectively. Z_w is the Warburg impedance related to the diffusion of lithium ions into the bulk electrode. The fitting values from this equivalent circuit are presented in Table 1. As it can be seen, the R_f and R_{ct}

Table 1. Kinetic Parameters of the N-MnO/GNS Electrode

sample	R_e (Ω)	R_f (Ω)	R_{ct} (Ω)	CPE_1 (F)	CPE_2 (F)
before cycling	2.3	312.1	113.3	2.1×10^{-5}	1.6×10^{-3}
after 10 cycles	3.5	106.9	26.1	7.9×10^{-5}	7.5×10^{-4}

of the N-MnO/GNS electrode after 10 cycles are 106.9 and 26.1 Ω, respectively, which are smaller than those of the initial

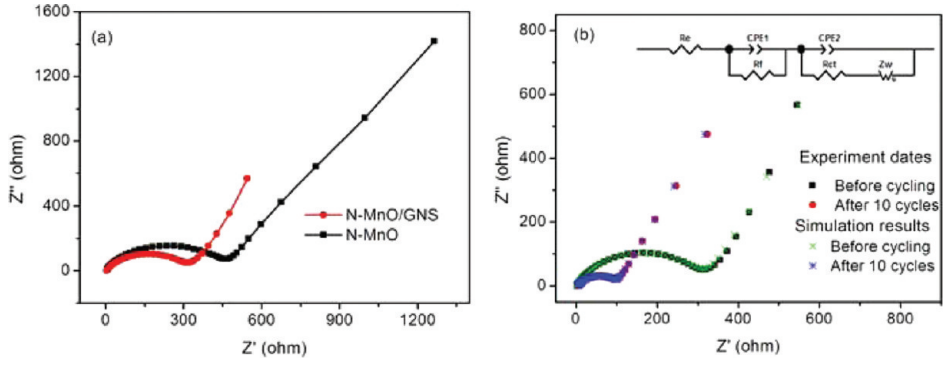

Figure 7. Nyquist plots of the N-MnO and N-MnO/GNS electrodes at 3.0 V (vs Li^+/Li) (a) before cycling and (b) N-MnO/GNS electrode after 10 cycles and the corresponding simulation results. Inset of b is the equivalent circuit used.

dx.doi.org/10.1021/am201173z | ACS Appl. Mater. Interfaces 2012, 4, 658−664

electrode (312.1 and 113.3 Ω). These results confirm that the incorporation of N-GNS can endow the N-MnO/GNS hybrid electrode with a high conductivity and greatly enhance electron transport during the electrochemical lithium insertion/extraction reaction.

Compared with the N-MnO and previously reported nanostructured MnO,[11−14,37] the enhanced capacity and cycle life of the N-MnO/GNS hybrid should be attributed to the unique N-doped nanostructure. As evidenced from the microscopic observation, the N-GNS serve as useful electronic framework for homogeneously dispersed N-MnO nanoparticles. The good mechanical flexibility of N-GNS in the hybrid not only readily accommodate the large volume change during conversion reaction but also efficiently prevent the aggregation of N-MnO.[20−23] Also, N-GNS serve as the conductive channels between N-MnO in the hybrid, which decrease the inner resistance of LIBs. In addition, N-doping could induce a large number of defects on the hybrid, which further enhance lithium storage properties.

CONCLUSIONS

N-MnO/GNS hybrid was synthesized by a simple hydrothermal method followed by heat treatment under ammonia atmosphere. The N-MnO nanoparticles are adhered to or embedded in N-GNS layers with a large number of surface defects induced by N-doping. Because of its unique N-doped nanostructure and efficiently mixed conducting network, the N-MnO/GNS hybrid exhibits large reversible capacity (772 mA h g^{-1} after 90 cycles), and a good rate capability (202 mA h g^{-1} at a high current density of 5 A g^{-1}) as an anode material. The N-MnO/GNS hybrid could be further explored as high capacity anode material for LIB application.

ASSOCIATED CONTENT

Supporting Information

SEM images of Mn_3O_4/graphene hybrid, H-MnO, N-MnO. XRD patterns of Mn_3O_4/graphene hybrid and H-MnO, XPS spectrum of N-MnO, UV−Vis spectra of the N-MnO and H-MnO. This material is available free of charge via the Internet at http://pubs.acs.org.

AUTHOR INFORMATION

Corresponding Author

*Fax: +86 532 80662744. E-mail: cuigl@qibebt.ac.cn.

ACKNOWLEDGMENTS

We appreciate the support of "100 Talents" program of the Chinese Academy of Sciences, National Program on Key Basic Research Project of China (973 Program) (MOST2011CB935700), Shandong Province Fund for Distinguished Young Scientist (BS2009NJ013), and National Natural Science Foundation of China (Grant 20971077).

REFERENCES

(1) Poizot, P.; Laruelle, S.; Grugeon, S.; Dupont, L.; Tarascon, J. M. *Nature* **2000**, *407*, 496−499.
(2) Varghese, B.; Reddy, M. V.; Zhu, Y. W.; Lit, C. S.; Hoong, T. C.; Rao, G. V. S.; Chowdari, B. V. R.; Wee, A. T. S.; Lim, C. T.; Sow, C. H. *Chem. Mater.* **2008**, *20*, 3360−3367.
(3) Wang, X. H.; Li, X. W.; Sun, X. L.; Li, F.; Liu, Q. M.; Wang, Qi.; He, D. Y. *J. Mater. Chem.* **2011**, *21*, 3571−3573.
(4) Nam, K. T.; Kim, D. P.; Yoo, J.; Chiang, C.; Meethong, N.; Hammond, P. T.; Chiang, Y.; Belcher, A. M. *Science* **2006**, *312*, 885−888.
(5) Lou, X. W.; Deng, D.; Lee, J. Y.; Feng, J.; Archer, L. A. *Adv. Mater.* **2008**, *20*, 258−262.
(6) Shi, Y. F.; Guo, B. K.; Corr, S. C.; Shi, Q. H.; H, Y. S.; Heier, K. R.; Chen, L. Q.; Seshadri, R.; Stucky, G. D. *Nano Lett.* **2009**, *9*, 4215−4220.
(7) Sun, Y. M.; Hu, X. L.; Luo, W.; Huang, Y. H. *ACS Nano* **2011**, DOI: 10.1021/nn201802c.
(8) Ban, C.; Wu, Z.; Gillaspie, D. T.; Chen, L.; Yan, Y.; Blackburn, J. L.; Dillon, A. C. *Adv. Mater.* **2010**, *22*, E145−E149.
(9) Zhang, W. M.; Wu, X. L.; Hu, J. S.; Guo, Y. G.; Wan, L. J. *Adv. Funct. Mater.* **2008**, *18*, 3941−3946.
(10) Fang, X. P.; Lu, X.; Wang, J. Z.; Wang, Z. X.; Wu, F.; Chen, L. Q. *Electrochem. Commun.* **2010**, *12*, 1520−1523.
(11) Zhi, L. J.; Hu, Y. S.; Hamaoui, B. E.; Wang, X.; Lieberwirth, I.; Kolb, U.; Maier, J.; Mullen, K. *Adv. Mater.* **2008**, *20*, 1727−1731.
(12) Poizot, P.; Laruelle, S.; Grugeon, S.; Dupont, L.; Tarascon, J. M. *J. Electrochem. Soc.* **2002**, *149*, A1212−A1216.
(13) Cui, G. L.; Gu, L.; Thomas, A.; Fu, L. J.; Antonietti, M.; Maier, J. *ChemPhysChem* **2010**, *11*, 3219−3223.
(14) Yu, X. Q.; He, Y.; Sun, J. P.; Li, H.; Chen, L, Q.; Huang, X. J. *Electrochem. Commun.* **2009**, *11*, 791−794.
(15) Yoo, E.; Kim, J.; Hosono, E.; Zhou, H.; Kudo, T.; Honma, I. *Nano Lett.* **2008**, *8*, 2277−2282.
(16) Wang, G. X.; Shen, X. P.; Yao, J.; Park, J. *Carbon* **2009**, *47*, 2049−2053.
(17) Novoselov, K. S.; Geim, A. K.; Morozov, S. V.; Dubonos, S. V.; Grigorieva, I. V.; Firsov, A. A. *Science* **2004**, *306*, 666−669.
(18) Rouhanipour, A.; Roy, M.; Feng, X. L.; Räder, H. J.; Müllen, K. *Angew. Chem., Int. Ed.* **2009**, *48*, 4602−4606.
(19) Balandin, A. A.; Ghosh, S.; Bao, W.; Calizo, I.; Teweldebrhan, D.; Miao, F.; Lau, C. N. *Nano Lett.* **2008**, *8*, 902−907.
(20) Paek, S. M.; Yoo, E. J.; Honma, I. *Nano Lett.* **2008**, *9*, 72−78.
(21) Yang, S. B.; Feng, X. L.; Ivanovici, S.; Müllen, K. *Angew. Chem., Int. Ed.* **2010**, *49*, 8408−8411.
(22) Zhou, G. M.; Wang, D. W.; Lu, G. Q.; Cheng, H. M. *Chem. Mater.* **2010**, *22*, 5306−5310.
(23) Wang, H. L.; Cui, L. F.; Yang, Y.; Dai, H. J. *J. Am. Chem. Soc.* **2010**, *132*, 13978−13980.
(24) Reddy, A. L. M.; Srivastava, A.; Gowda, S. R.; Gullapalli, H.; Dubey, M.; Ajayan, P. M. *ACS Nano* **2010**, *4*, 6337−6342.
(25) Wang, H. B.; Zhang, C. J.; Wang, L.; Han, P. H.; Cui, G. L. *J. Mater. Chem.* **2011**, *21*, 5430−5435.
(26) Deifallah, M.; McMillan, P. F.; Cora, F. *J. Phys. Chem. C.* **2008**, *112*, 5447−5451.
(27) Wehling, T. O.; Novoselov, K. S.; Morozov, S. V.; Vdovin, E. E.; Katsnelson, M. I.; Geim, A. K.; Lichtenstein, A. I. *Nano Lett.* **2008**, *8*, 173−177.
(28) Hummers, W. S.; Offeman, R. E. *J. Am. Chem. Soc.* **1958**, *80*, 1339−1341.
(29) Chen, S.; Zhu, J. W.; Wang, X. *ACS Nano* **2010**, *4*, 2822−2827.
(30) Maleservic, A.; Vitchev, R.; Schouteden, K.; Volodin, A.; Zhang, L.; Tendeloo, G. V.; Vanhulsel, A.; Haesendonck, C. V. *Nanotechnology* **2008**, *19*, 305604−3095607.
(31) Yang, Q. H.; Hou, P. X.; Unno, M.; Yamauchi, S.; Saito, R.; Yotani, T. K. *Nano Lett.* **2005**, *5*, 2465−2469.
(32) Jafri, R. I.; Rajalakshmi, N.; Ramaprabhu, S. *J. Mater. Chem.* **2010**, *20*, 7114−7117.
(33) Li, B. X.; Rong, G. X.; Xie, Y.; Huang, L. F.; Feng, C. Q. *Inorg. Chem.* **2006**, *45*, 6404−6410.
(34) Zhang, C. H.; Fu, L.; Liu, N.; Liu, M. H.; Wang, Y. Y.; Liu, Z. F. *Adv. Mater.* **2011**, *23*, 1020−1024.
(35) Ma, T.; Akiyama, M.; Abe, E.; Imai, I. *Nano Lett.* **2005**, *5*, 2543−2549.
(36) Qiu, X. F.; Burda, C. *Chem. Phys.* **2007**, *339*, 1−10.
(37) Zhong, K. F.; Xia, X.; Zhang, B.; Li, H.; Wang, Z. X.; Chen, L. Q. *J. Power Sources* **2010**, *195*, 3300−3307.

(38) Grugeon, S.; Laruelle, S.; Dupont, L.; Tarascon, J. M. *Solid State Sci.* **2003**, *5*, 895−904.
(39) Jiang, H.; Yang, L. P.; Li, C. Z.; Yan, C. Y.; Lee, P. S.; Ma, J. *Energy Environ. Sci.* **2011**, *4*, 1813−1819.
(40) Xiang, H. F.; Zhang, K.; Ji, G.; Lee, J. Y.; Zou, C. J.; Chen, X. D. *Carbon* **2011**, *49*, 1787−1796.
(41) Zhang, K. J.; Wang, H. B.; He, X. Q.; Liu, Z. H.; Gu, L.; Xu, H. X.; Dong, S. M.; Han, P. X.; Cui, G. L.; Chen, L. Q.; et al. *J. Mater. Chem.* **2011**, *21*, 11916−11922.